Advanced Optical Materials

ADVANCED OPTICAL MATERIALS
www.advopticalmat.de

RESEARCH ARTICLE

Synergistic Piezophototronic and Bandgap Engineering in a Flexible $MoTe_2/In_2Se_3$ Heterojunction Photodetector

Qingyan Deng[1,2] | Yuting Ye[1,2] | Jialing Jian[1,3] | Jianghong Wu[1,2] | Yinyin Song[1,2] | Hui Ma[4] | Hongtao Lin[4] | Lan Li[1,2,5]

[1]Zhejiang Key Laboratory of 3D Micro/Nano Fabrication and Characterization, Department of Electronic and Information Engineering, School of Engineering, Westlake University, Hangzhou, China | [2]Institute of Advanced Technology, Westlake Institute for Advanced Study, Hangzhou, China | [3]School of Integrated Circuits, Jiangnan University, Wuxi, China | [4]State Key Laboratory of Brain-Machine Intelligence, College of Information Science and Electronic Engineering, Zhejiang University, Hangzhou, China | [5]Westlake Institute for Optoelectronics, Fuyang, Hangzhou, China

Correspondence: Lan Li (lilan@westlake.edu.cn)

Received: 21 May 2026 | **Revised:** 7 August 2026 | **Accepted:** 23 August 2026

Keywords: optoelectronics | photodetector | piezoelectricity | strain engineering | van der waals heterostructures

ABSTRACT

Two-dimensional materials provide a versatile platform for flexible optoelectronics. However, previous strain-engineered flexible photodetectors have generally exhibited a narrow spectral range, with most studies focusing solely on the visible range and lacking broadband response capability. Here, we present a flexible photodetector based on the $MoTe_2/In_2Se_3$ van der Waals heterojunction, where the piezophototronic effect and strain-induced bandgap modulation are combined to achieve a strain-enhanced broadband response from the visible to the short-wave infrared. Under controlled uniaxial tensile strain, the induced piezo-potential within the heterojunction significantly enhances the built-in electric field at the interface, while the strain-reduced bandgap of $MoTe_2$ synergistically promotes photocarrier generation and separation. Consequently, the device exhibits a broadband photoresponse and pronounced responsivity enhancements of 191% at 638 nm and 260% at 1310 nm under optimized tensile strain, along with an ultralow dark current of 9.4 pA. These results demonstrate an effective strain-modulated photon-to-electron transition in flexible van der Waals heterostructures and offer a viable strategy for designing high-performance flexible optoelectronic devices.

1 | Introduction

Flexible photodetectors, as essential components in flexible optoelectronic circuits [1–3], have garnered broad research interest for their promising applications in optical interconnects [4, 5], health monitoring [6–8], and image sensors [9–11]. Free from the constraints of physical rigidity, flexible photodetectors can conform intimately to various curved and contoured surfaces in their working environments. This inherent adaptability further enables stable operation under diverse mechanical deformations, including bending, stretching, or even twisting, while simultaneously processing complex and variable optical signals in real-time [12–14]. Among various photoactive materials [15, 16], 2D materials (2DMs) have emerged as a promising platform for constructing high-performance flexible photodetectors, owing to their atomic-scale thickness, exceptional mechanical flexibility, and tunable band-structure diversity [17–24]. Moreover, their integration on flexible substrates eliminates lattice-matching constraints inherent to bulk semiconductors, enabling versatile manipulation of band structures and carrier transport [25, 26].

Extensive research on flexible photodetectors has predominantly focused on maintaining device performance under mechanical deformation [27–31]. Intrinsic strain in flexible architectures induces modulation of optoelectronic characteristics by piezophototronic effect [32–37], strain-induced bandgap modulation [38–43], and the strain-enhanced photovoltaic effect [44]. Although previous studies have demonstrated a strain-induced enhancement in photodetector responsivity, the underlying mechanisms regulating device performance remain largely empirical and lack systematic analysis. Furthermore, the reported flexible photodetectors generally exhibited limited spectral coverage, with most operating effectively only in the visible range. In the short-wave infrared (SWIR) range, where light exhibits strong tissue penetration and low scattering, such devices are pivotal for biomedical imaging [45] and optical integrated sensing and communication [46]. Therefore, it is imperative to rationally design flexible photodetectors based on fundamental physical principles, which demonstrate broadband response from the visible to the SWIR.

To address these challenges, we designed a $MoTe_2/In_2Se_3$ van der Waals heterojunction to harness the multiple strain-responsive principles. Although $MoTe_2/In_2Se_3$ heterostructures have demonstrated potential for multicolor and polarization-sensitive photodetection, the impact of mechanical strain on their optoelectronic properties remains largely unexplored [47]. $MoTe_2$, a representative transition metal dichalcogenide material with an indirect bandgap of ~1.04 eV, exhibits intrinsic infrared absorption with a cutoff near 1192 nm. Under tensile strain, its bandgap can be narrower, enabling longer-wavelength absorption. In contrast, In_2Se_3 exhibits strong piezoelectricity, enabling the generation and distribution of piezoelectric charges under strain [36–38]. In the flexible photodetector, these mechanisms act cooperatively under controlled uniaxial tensile strain. The strain amplifies the built-in field via the In_2Se_3 piezopotential and reduces the $MoTe_2$ bandgap, which in turn boosts the generation of photoinduced carriers and facilitates their separation. As a result, the obtained photodetector exhibits a broadband, strain-enhanced photoresponse from the visible to the SWIR. Under optimized tensile strain, it exhibited pronounced responsivity enhancement of 191% at 638 nm and 260% at 1310 nm, along with a significantly suppressed dark current of 9.4 pA and a high specific detectivity of 3.20×10^9 Jones. This synergistic strain-engineering strategy establishes a general pathway for designing flexible, high-sensitivity broadband photodetectors by combining bandgap-tunable and piezo-responsive 2DMs in van der Waals heterostructures.

2 | Results and Discussion

A flexible photodetector based on a $MoTe_2/In_2Se_3$ vertical van der Waals heterostructure was fabricated on a polyimide substrate, as illustrated in Figure 1a. The corresponding layered architecture of the device is shown in Figure 1b. Fabrication started by planarizing the polyimide substrate with the SU-8 layer and depositing Ti/Au (5/25 nm) electrodes via e-beam evaporation. We then used a PDMS-assisted dry transfer method to vertically stack mechanically exfoliated $MoTe_2$ and In_2Se_3 flakes onto the electrodes. Finally, an hBN capping layer and an SU-8 encapsulation layer protected the heterostructure and enhanced its stability. Raman spectroscopy was employed to confirm the composition and structural quality of the constituent materials and the prepared heterostructure (Figure 1c). The $MoTe_2$ nanoflake exhibits characteristic Raman peaks at 173 cm^{-1} (A_{1g}, out-of-plane) and 233 cm^{-1} (E_{2g}, in-plane), confirming its 2H phase. Meanwhile, the α-In_2Se_3 spectrum displayed distinct peaks at 88 cm^{-1} (E mode, symmetric phonon vibrations), 104 cm^{-1} (A_1(LO+TO)), 180 cm^{-1} (A_1(LO)), and 194 cm^{-1} (A_1(TO)), where the A_1(LO) and A_1(TO) modes originate from longitudinal-transverse optical splitting [47–50]. In the overlapping region of the heterostructure, the presence of well-resolved Raman peaks from both 2H-$MoTe_2$ and α-In_2Se_3 provides evidence of its successful preparation via mechanical stacking. Furthermore, the negligible defect peaks suggest a high-quality interface.

Atomic force microscopy (AFM) reveals the thickness of the transferred flakes, with $MoTe_2$ and In_2Se_3 showing multilayer thicknesses of approximately 58 and 62 nm, respectively (Figure S1). To further probe the interfacial electronic properties, we conducted Kelvin probe force microscopy (KPFM, Figure 1d). According to the KPFM measurements, In_2Se_3 exhibits a higher surface potential than $MoTe_2$, indicating a smaller work function. Upon contact, electrons transfer from In_2Se_3 to $MoTe_2$ until Fermi-level equilibration, leading to the formation of a depletion region and a built-in electric field directed from In_2Se_3 toward $MoTe_2$. The measured surface potential difference of ~160 mV further confirms the work function difference and supports the formation of the interfacial built-in field (Figure 1e). Furthermore, the p-type and n-type semiconducting behaviors of $MoTe_2$ and In_2Se_3 were verified through the transfer characteristics of corresponding field-effect transistors fabricated on SiO_2/n^+-Si substrates (Figure 1f) [49, 50]. The complementary p-type and n-type characteristics indicate that stacking these two materials forms a p-n junction at the heterointerface. This conclusion is further supported by the rectifying behavior observed in the dark current–voltage (I–V) characteristics (Figure S2). Based on this curve, the ideality factor extracted from the forward-bias region using the Shockley diode model [35, 36] is $n = 3.95$ (Figure S4). A detailed discussion of the ideality factor is provided in Section S4.

Building on the structural and interfacial characterizations, we systematically investigated the photoresponse characteristics of the flexible $MoTe_2/In_2Se_3$ heterojunction photodetector. The photodetector was initially characterized under unstrained conditions, exhibiting a broadband photoresponse from the visible to the SWIR. We measured the current–voltage (I–V) characteristics under 638 nm illumination with optical power ranging from 12 nW to 380 μW (Figure 2a). The depletion layer at the van der Waals heterojunction interface effectively suppresses dark current, resulting in an ultralow value of 9.4 pA under a reverse bias of −2 V. Moreover, the presence of the heterojunction structure enables a distinct self-powered photocurrent under 638 nm illumination, which increases markedly with rising optical power (Figure S2). Meanwhile, the device exhibits a pronounced photoresponse under both forward- and reverse-bias conditions. The photocurrent increases consistently with incident optical power, attributed to the increased number of photogenerated carriers at higher excitation intensities. The relationship between photocurrent and optical power under 638 nm illumination was extracted at bias voltages of −2 and 2 V, as shown in the left panel of Figure 2b. An approximately linear correlation between photocurrent and incident optical power (ranging from 12 nW to 380 μW) is observed on a logarithmic scale. The responsivity (R), shown in the right panel of Figure 2b and calculated as $R = I_{ph}/P_{in}$ (I_{ph} and P_{in} denote photocurrent and incident optical power, respectively), reaches 20.8 mA/W at −2 V and 347.7 mA/W at 2 V

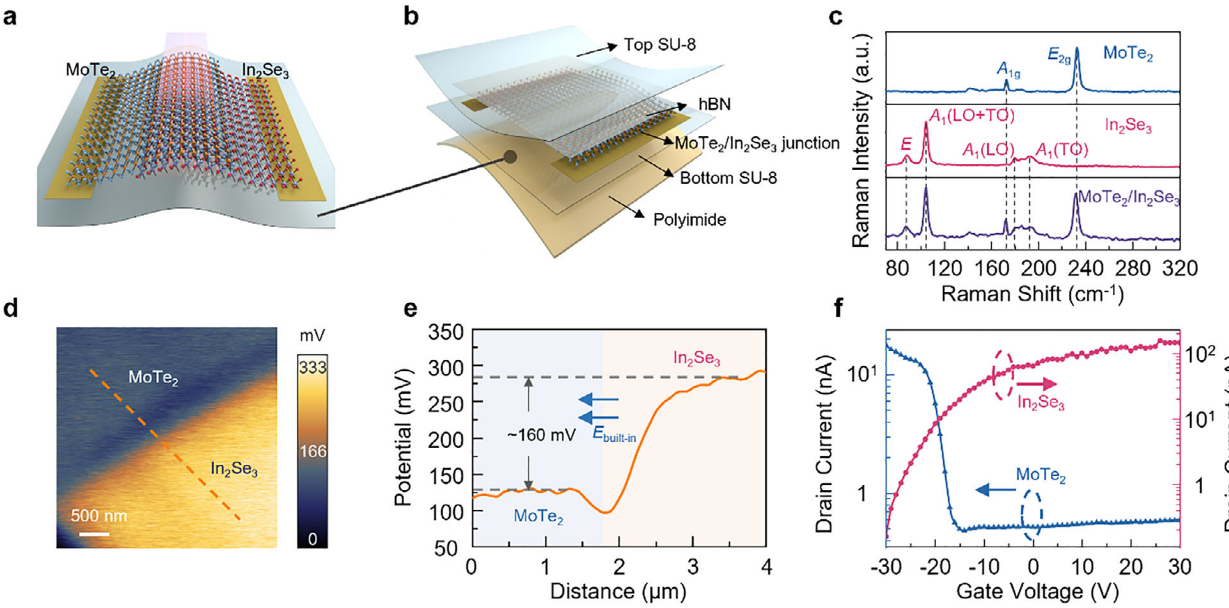

FIGURE 1 | Device geometry and characterization of $MoTe_2/In_2Se_3$ heterojunction flexible photodetector. (a) Schematic of the $MoTe_2/In_2Se_3$ heterojunction photodetector on the polyimide substrate. (b) Schematic of the layered architecture of a flexible $MoTe_2/In_2Se_3$ heterojunction photodetector. (c) Raman spectra of an isolated $MoTe_2$ flake, an In_2Se_3 flake, and the formed $MoTe_2/In_2Se_3$ heterojunction. (d) KPFM measurement of the surface potential across the $MoTe_2/In_2Se_3$ heterojunction. (e) Line profile of the KPFM potential along the dashed line in (d). (f) Transfer characteristics of $MoTe_2$ and In_2Se_3 field effect transistors at a bias voltage of 0.5 V.

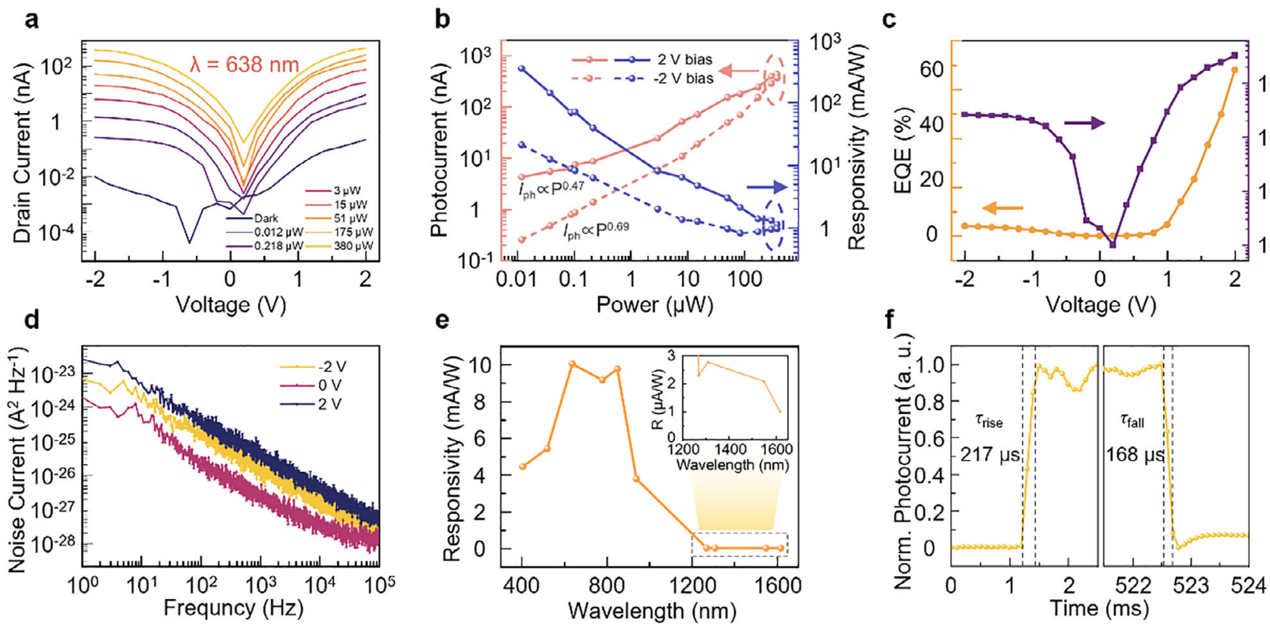

FIGURE 2 | Optoelectronic characterization of the $MoTe_2/In_2Se_3$ heterojunction photodetector at 638 nm. (a) *I–V* curves of the $MoTe_2/In_2Se_3$ photodetector under 638 nm illumination with varying optical power. (b) Measured photocurrent and calculated responsivity as a function of optical power at bias voltages of −2 and 2 V, respectively. (c) Corresponding external quantum efficiency (EQE) and specific detectivity (D^*) calculated based on the noise spectral density at 1750 Hz. (d) Current noise spectral density as a function of frequency under different bias voltages. (e) Spectral responsivity across different wavelengths. Inset: magnified view of the responsivity in the SWIR region. (f) Temporal photoresponse measured at a 2 V bias.

under an incident power of 12 nW, indicating efficient photon-to-electron conversion. The R variation is attributed to trap states in the $MoTe_2/In_2Se_3$ heterojunction [51–53]. These trap states generally possess a limited density of states. Thus, under low light intensity, they contribute dominantly to the generation of photo-induced carriers, leading to high responsivity. However, as the incident optical power increases, the trap states become saturated, resulting in a decrease in responsivity. To further understand the carrier generation and recombination dynamics, the I_{ph} dependence on incident optical power was analyzed using the power-law relationship $I_{ph} = AP^{\alpha}$, where A is a proportionality constant, P is the incident optical power, and α is the power-law exponent that reflects the carrier generation and recombination dynamics [37, 54]. The extracted α values are 0.69 at −2 V and 0.47 at +2 V, indicating a sublinear dependence of photocurrent on incident optical power (Figure S5).

The external quantum efficiency (EQE) of the photodetector under 12 nW illumination at 638 nm was calculated as a function of V_{ds} using the equation EQE = $Rhc/q\lambda$ (where h is Planck's constant, c is the light speed, q is the elementary electron charge, and λ is the wavelength). As shown in Figure 2c (orange line), the device exhibits an EQE of 67.6% at 2 V and 4.1% at −2 V, demonstrating its effective photoresponse under both forward and reverse bias. Meanwhile, the specific detectivity (D^*) can be calculated using the equation $D^* = R \cdot \frac{\sqrt{A_d \cdot \Delta f}}{i_n}$, where A_d is the effective area of the photodetector, Δf is the bandwidth, and i_n is the noise current originating from 1/f noise, shot noise, and thermal noise. We also measured noise spectral density of the $MoTe_2/In_2Se_3$ photodetector (Figure 2d), which reveals characteristic 1/f noise that follows the Hooge empirical relation: $S_f = A \cdot i^{\alpha}/f^{\beta}$ (i, f and A represent the channel current, frequency, and noise amplitude, respectively). At a bias of −2 V, the measured shot noise and thermal noise are 3.34×10^{-30} A^2/Hz and 8.89×10^{-32} A^2/Hz, respectively. As shown in Figure 2d, the 1/f noise serves as the dominant noise source within the measured frequency range, with its magnitude being at least two orders of magnitude higher than that of the shot noise and thermal noise. Therefore, the 1/f noise becomes the dominant factor limiting the detection sensitivity of the device in the low-frequency regime. Benefiting from the low dark current and suppressed noise characteristics of the heterojunction structure, the device achieves high specific detectivity values of 2.60×10^8 Jones at −2 V and 3.20×10^9 Jones at 2 V, as presented in the right panel of Figure 2c (purple line).

As shown in Figure 2e, the device operates over a spectral range from 405 to 1620 nm, spanning wavelengths from the visible to the SWIR region. It exhibits peak responsivity at 638 nm, corresponding to its maximum external quantum efficiency. This spectral response is attributed to the dispersion relation and the collection efficiency of photogenerated carriers. The inset of Figure 2e reveals a weak but discernible photoresponse in the SWIR region, with responsivity values of 2.76 µA/W at 1310 nm and 2.08 µA/W at 1550 nm. Furthermore, the dynamic photoresponse of this photodetector was evaluated under a 2 V bias. As displayed in Figure 2f, the rise and decay times were measured to be 217 and 168 µs, respectively.

To investigate the effect of strain on the photoresponse of the $MoTe_2/In_2Se_3$ heterojunction photodetector, we applied tensile strain to the flexible device using a custom-built testing stage (Figure S3). By optimizing the device structure through finite element simulations, we determined the thicknesses of the polyimide substrate and SU-8 layer required to apply sufficient strain to the $MoTe_2/In_2Se_3$ heterojunction. As shown in Figure 3a, one of the strain configurations employed during testing is illustrated. When the film is compressed inward from both sides by the stage, the central region of the film arches upward, generating tensile strain in the upper surface. 2DMs were precisely fabricated in this central region to ensure effective strain modulation. In addition, as shown earlier in Figure 1b, the heterostructure was encapsulated with an hBN layer and a top SU-8 film to protect the materials during deformation. The cross-sectional view along the x-z plane (Figure 3b) provides structural details of the configuration presented in Figure 3a. The region between the white and black dashed lines represents the bottom SU-8 layer in Figure 1b, while the area above the black dashed line corresponds to the top SU-8 encapsulation. The active device is located along the black dashed line, where the simulated in-plane x-direction tensile strain (ε_x) reaches 0.91%.

We measured the dependence of the photodetector's dark current on applied strain under a −2 V bias and plotted the results in Figure 3c. As the applied tensile strain increases, the dark current rises progressively from 9.4 pA at 0% strain to 15.3 pA at 0.91% strain, corresponding to an increase of approximately 63%. This clear strain-dependent behavior demonstrates the effective modulation of the dark current by tensile strain. The increase can be attributed to the strain-induced bandgap narrowing in $MoTe_2$. The reduced bandgap lowers the carrier excitation energy, thereby enhancing thermal generation and resulting in higher dark current [38, 42]. The photoresponse of the device was characterized under a bias voltage of −2 V by varying both the optical power and the applied tensile strain across the visible-to-SWIR wavelength range. As shown in Figure 3d,e, the device responsivity increases with applied strain from 0% to approximately 1% under both 638 and 1310 nm illumination. Under 638 nm illumination with an optical power of 13 nW, the responsivity rises from 10 mA/W in the flat state to 29.10 mA/W at 0.91% tensile strain, corresponding to an enhancement of 191% (yellow solid line in Figure 3f). In addition to this strain-enhanced photoresponse in the visible region, a similar effect is observed in the SWIR range at wavelengths such as 940 nm (Figure S3) and 1310 nm. Under 1310 nm illumination with an optical power of 42.76 µW, the responsivity increases from 0.30 to 1.08 µA/W at 1.09% tensile strain, corresponding to an enhancement of 260% (blue solid line in Figure 3f). These results clearly demonstrate that the photoresponse of the device can be effectively modulated by applied tensile strain. The opposite modulation behavior under compressive strain was also experimentally verified (Figure S8), further confirming the strain-dependent tunability of the device.

To further elucidate the modulation mechanism of the piezophototronic effect on device performance, schematic energy band diagrams of the $MoTe_2/In_2Se_3$ heterojunction under varying tensile strain conditions are presented in Figure 4. The direct contact between $MoTe_2$ (bandgap: ~1.04 eV) [42, 55] and In_2Se_3 (bandgap: ~1.6 eV) [47, 56], combined with their work function characteristics, leads to the formation of a type-II band alignment in the van der Waals heterostructure [57, 58]. This band alignment is further confirmed by the diode-like behavior observed in the current-voltage characteristics measured under dark conditions (Figure S2).

Under equilibrium conditions with no illumination or strain, the p–n heterojunction between p-type $MoTe_2$ and n-type In_2Se_3 exhibits a characteristic band alignment, as shown in Figure 4a. The established built-in electric field at the interface balances

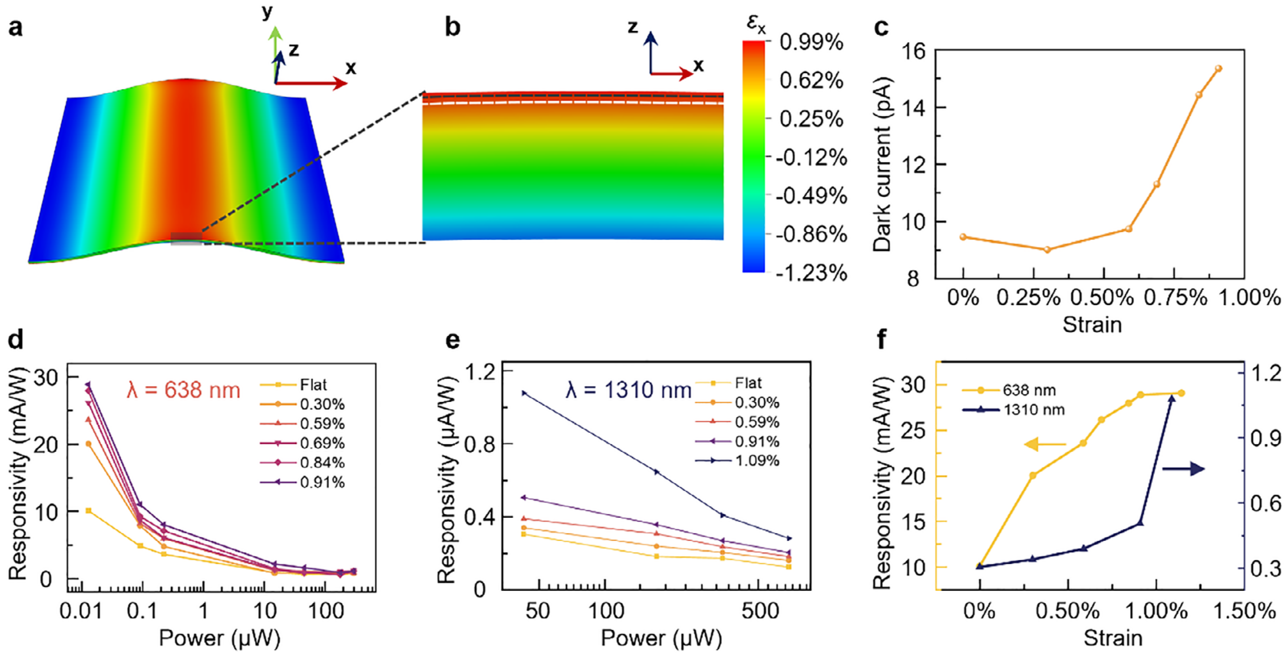

FIGURE 3 | Strain-enhanced photoresponse of the flexible $MoTe_2/In_2Se_3$ heterojunction photodetector. (a) Simulated in-plane x-direction strain (ε_x) distribution in the flexible photodetector under bending. (b) Corresponding cross-sectional view of the simulation; the white and black dashed lines mark the polyimide/SU-8 interface and the $MoTe_2/In_2Se_3$ heterojunction, respectively. (c) Dark current of the $MoTe_2/In_2Se_3$ heterojunction photodetector as a function of applied strain at −2 V. (d,e) Responsivity as a function of optical power and strain at (d) 638 nm and (e) 1310 nm wavelength. The color darkness represents the magnitude of the applied strain. (f) Strain-dependent responsivity under 0.013 μW at 638 nm and 42.76 μW at 1310 nm illumination.

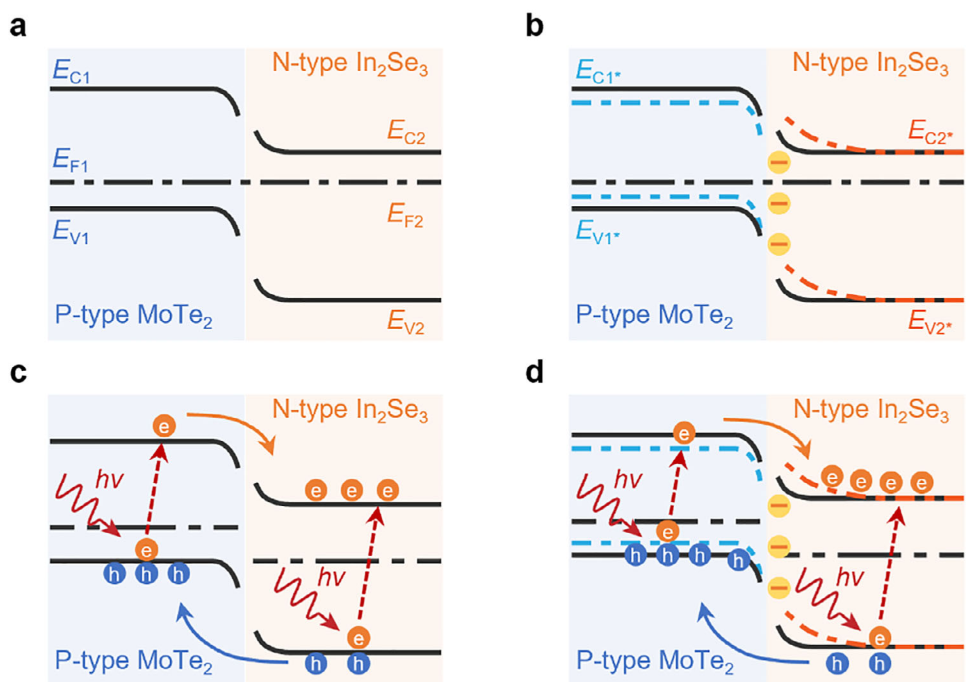

FIGURE 4 | Energy band diagrams of the $MoTe_2/In_2Se_3$ heterojunction under various strain and illumination conditions. (a,b) Diagrams at thermal equilibrium without illumination: (a) before and (b) after applying tensile strain. (c,d) Under light illumination: (c) before and (d) after applying tensile strain. In all diagrams, the black, light blue, and orange dashed lines represent the Fermi level and the energy levels of strained $MoTe_2$ and In_2Se_3, respectively. E_C, E_F, and E_V denote the conduction band, Fermi level, and valence band.

the drift and diffusion currents, resulting in equilibrium. In the diagrams, the black solid lines denote the conduction band (E_C) and valence band (E_V) of $MoTe_2$ and In_2Se_3, respectively. The black dashed line represents the Fermi level across the heterojunction. The subscripts "1" and "2" are used to label the bands corresponding to $MoTe_2$ and In_2Se_3, respectively.

When tensile strain is applied to the van der Waals heterostructure, the band structures of both materials are modified. As depicted in Figure 4b, light blue and orange dashed lines represent the energy levels of strained $MoTe_2$ and In_2Se_3, respectively. First, tensile strain generates negative piezoelectric polarization charges at the heterojunction interface in the In_2Se_3 layer. This originates from the non-centrosymmetric crystal structure of In_2Se_3, wherein mechanical deformation causes lattice distortion and a consequent reorientation of the polarization vector [37]. The resulting piezo-potential fundamentally alters the electrostatic landscape of the junction. According to the theory of piezotronics [59–61], negative polarization charges at the n-type semiconductor interface reduce the depletion width on the p-type side ($MoTe_2$), while simultaneously expanding and shifting the depletion region toward the n-type side (In_2Se_3). This redistribution of charge induces pronounced upward band bending in the In_2Se_3 side near the interface. Consequently, the realigned energy band profile, characterized by a steeper band slope, effectively reduces the energy barrier for carrier transport and enhances the built-in electric field, thereby facilitating the separation and extraction of photogenerated carriers. Second, as predicted by first-principles density functional theory calculations [42], tensile strain modifies the band structure of $MoTe_2$: the valence band maximum at the Γ point shifts to higher energy, while the conduction band minima at the K and H points shift to lower energy and become degenerate. This results in a net reduction of the bandgap, as depicted by the light blue dashed lines in Figure 4b. The reduced bandgap lowers the energy required for carrier excitation, which promotes thermal generation and consequently leads to an increase in dark current. This mechanism explains the experimental trend shown in Figure 3c, where the dark current rises with increasing strain as the bandgap narrows. Additional KPFM measurements on mechanically deformed regions were performed to further support the proposed modulation mechanism (Figure S7).

Under optical illumination with a penetration depth exceeding the junction thickness (Figure 4c), photogenerated electron-hole pairs are separated by the built-in electric field. The resulting free carriers then drift across the depletion region, with electrons moving toward In_2Se_3 and holes toward $MoTe_2$. This process generates an external photocurrent. When tensile strain is applied to the heterostructure under illumination (Figure 4d), the combined effects of the piezo-potential in In_2Se_3 and the bandgap reduction of $MoTe_2$ suppress electron-hole pair recombination while enhancing carrier separation efficiency near the heterointerface. This synergistic mechanism leads to a significant enhancement in both photocurrent and responsivity across the visible-to-SWIR wavelength range, yielding maximum responsivity improvements of 191% at 638 nm and 260% at 1310 nm, as shown in Figure 3f.

3 | Conclusion

In summary, we have fabricated a flexible photodetector based on a $MoTe_2/In_2Se_3$ heterojunction to investigate the synergistic influence of piezophototronic effect and strain-induced bandgap modulation on strain-modulated photodetection. Under illumination from the visible to the SWIR range, strain-induced steepening of the band slope in In_2Se_3 and concurrent bandgap reduction in $MoTe_2$ collectively lower the carrier transport barrier and enhance the built-in electric field. This promotes efficient separation and collection of photogenerated carriers, directing holes toward $MoTe_2$ and electrons toward In_2Se_3, thereby increasing the photocurrent. In the unstrained state under 638 nm illumination and 12 nW incident power, the photodetector achieves a responsivity of 347.7 mA/W, a specific detectivity of 3.20×10^9 Jones, and a dark current of 9.4 pA. Under tensile strain, the cooperative action of the In_2Se_3 piezophototronic effect and the strain-tunable bandgap of $MoTe_2$ modulates the heterojunction band structure, leading to an enhanced photoresponse across the visible-to-SWIR spectrum. Experimental results demonstrate that under tensile strain, the responsivity increases by 191% at 638 nm and 260% at 1310 nm. These findings confirm the effective strain-mediated modulation of the photoresponse in flexible $MoTe_2/In_2Se_3$ photodetectors and establish an important foundation for the development of flexible optoelectronic devices.

4 | Experimental Section

4.1 | Device Fabrication

The fabrication began with a 100 μm-thick polyimide film serving as the substrate for the entire device. This was followed by spin-coating a ∼5 μm SU-8 layer for surface planarization. Next, the metal contact regions were defined by UV lithography. A Ti/Au bilayer (5/25 nm) was subsequently deposited via electron-beam evaporation (ULVAC Ei-5Z) and patterned into electrodes using a standard lift-off process. Multilayer flakes of $MoTe_2$ and In_2Se_3 were mechanically exfoliated from bulk crystals (Taizhou SUNANO New Energy Co., Ltd.) with Scotch tape. These flakes were then aligned and transferred onto the substrate using a polydimethylsiloxane (PDMS) stamp and a custom-built transfer stage to form the heterojunction. Finally, an hBN capping layer was applied to improve device stability, and the device was encapsulated with a ∼3 μm-thick SU-8 layer. The encapsulated device film was mounted onto a custom-built translation stage. This stage consists of two platforms whose separation can be independently adjusted via micrometer knobs. By fixing one platform and rotating the knob on the other to reduce the inter-platform distance, the film was bent upward, thereby applying a substantial strain to the $MoTe_2/In_2Se_3$ heterojunction.

4.2 | Device Characterizations

Atomic force microscopy (Oxford Instruments, Jupiter XR) was employed to investigate the morphology and surface potential of the $MoTe_2/In_2Se_3$ heterojunction. Raman spectroscopy (WITec, Alpha300R) was used to assess the material quality of the exfoliated $MoTe_2$ and In_2Se_3 flakes. For electrical characterization, the device was first packaged by vertically bonding its electrodes to the pins of a flexible printed circuit board using conductive adhesive. This approach effectively minimized the influence of the strain-applying apparatus on electrical measurements. The static optoelectronic response was then measured using a semiconductor parameter analyzer (PDA, FS-Pro) under illumination from fiber lasers (wavelength range: 405–1620 nm). To measure the response speed, the signal generator (Siglent, SDG6032X-E) modulated the laser to produce a square-wave signal. The transient electrical responses of the device were recorded using the high-speed sampling module of the semiconductor parameter analyzer (PDA, FS-Pro) and a sampling oscilloscope (Anritsu, MP1900A). A detailed description and schematic illustration of the optical and electrical measurement system are provided in Section S11. The optical power calibration procedure and optical alignment process during measurements are described in Section S12.

Author Contributions

L.L. conceived the study. Q.D. designed and fabricated the devices and performed the measurements. Y.Y. contributed to the experimental design and the electrical packaging of the devices. Y.Y., J.J., J.W., and H.M. contributed to the characterization of the optoelectronic properties. Y.Y., J.J., J.W., Y.S., and H.M. contributed to the analysis and presentation of the results. Q.D. analyzed the data and prepared the manuscript draft. L.L. and H.L. supervised and coordinated the project. All authors discussed the results and commented on the manuscript.

Acknowledgements

The authors thank the Westlake Center for Micro/Nano Fabrication and Instrumentation and the Service Center for Physical Sciences and Molecular Sciences at Westlake University for facility support, and the ZJU Micro-Nano Fabrication Center at Zhejiang University. The research was partially supported by "Pioneer" and "Leading Goose" R&D Program of Zhejiang Province (2024SDXHDX0005), Key R&D Program of Zhejiang Province (2024C03150), National Natural Science Foundation of China (Grant Numbers 12104375), and Key Project of Westlake Institute for Optoelectronics (2023GD003/110500Y0022303).

Conflicts of Interest

The authors declare no conflict of interest.

Data Availability Statement

The data that support the findings of this study are available from the corresponding author upon reasonable request.

References

1. H. M. Schrickx, S. Gyurek, C. Moore, et al., "Flexible Self-Powered Organic Photodetector With High Detectivity for Continuous On-Plant Sensing," *Advanced Optical Materials* 12, no. 18 (2024): 2400005, https://doi.org/10.1002/adom.202400005.

2. Y. Chen, Z. Song, H. Liang, et al., "Amorphous Tellurium–Selenium Alloy: A Promising Candidate Material Toward Broadband Optoelectronics," *Laser & Photonics Reviews* 19, no. 23 (2025): 00586, https://doi.org/10.1002/lpor.202500586.

3. Y. Zhu, Z. Zhang, H. Qin, et al., "Flexible and High-Performance Solution-Processable Single-Detector Organic Spectrometer," *Advanced Materials* 37, no. 33 (2025): 2502608, https://doi.org/10.1002/adma.202502608.

4. Y. Ye, H. Ma, J. Wu, et al., "Flexible InGaAs Photodetector with High-Speed Detection and Long-Term Stability," *IEEE Journal of Selected Topics in Quantum Electronics* 30 (2024): 1–8.

5. L. Li, Y. Zou, H. Lin, et al., "A Fully-Integrated Flexible Photonic Platform for Chip-to-Chip Optical Interconnects," *Journal of Lightwave Technology* 31, no. 24 (2013): 4080–4086, https://doi.org/10.1109/JLT.2013.2285382.

6. E. O. Polat, G. Mercier, I. Nikitskiy, et al., "Flexible Graphene Photodetectors for Wearable Fitness Monitoring," *Science Advances* 5, no. 9 (2019): aaw7846, https://doi.org/10.1126/sciadv.aaw7846.

7. Y. Tang, P. Jin, Y. Wang, et al., "Enabling Low-drift Flexible Perovskite Photodetectors by Electrical Modulation for Wearable Health Monitoring and Weak Light Imaging," *Nature Communications* 14, no. 1 (2023): 4961, https://doi.org/10.1038/s41467-023-40711-1.

8. K. Mahato, T. Saha, S. Ding, S. S. Sandhu, A.-Y. Chang, and J. Wang, "Hybrid Multimodal Wearable Sensors for Comprehensive Health Monitoring," *Nature Electronics* 7, no. 9 (2024): 735–750, https://doi.org/10.1038/s41928-024-01247-4.

9. C. Choi, M. K. Choi, S. Liu, et al., "Human Eye-Inspired Soft Optoelectronic Device Using High-Density MoS_2-Graphene Curved Image Sensor Array," *Nature Communications* 8, no. 1 (2017): 1664, https://doi.org/10.1038/s41467-017-01824-6.

10. L. Gu, S. Poddar, Y. Lin, et al., "A Biomimetic Eye With a Hemispherical Perovskite Nanowire Array Retina," *Nature* 581, no. 7808 (2020): 278–282, https://doi.org/10.1038/s41586-020-2285-x.

11. Y. Ye, Q. Deng, J. Wu, et al., "Electrostatic Force-Assisted Transfer of Flexible Silicon Photodetector Focal Plane Arrays for Image Sensors," *ACS Applied Materials & Interfaces* 16, no. 30 (2024): 39572–39579, https://doi.org/10.1021/acsami.4c05890.

12. Q.-B. Zhu, B. Li, D.-D. Yang, et al., "A Flexible Ultrasensitive Optoelectronic Sensor Array for Neuromorphic Vision Systems," *Nature Communications* 12, no. 1 (2021): 1798, https://doi.org/10.1038/s41467-021-22047-w.

13. S. Chang, J. H. Koo, J. Yoo, et al., "Flexible and Stretchable Light-Emitting Diodes and Photodetectors for Human-Centric Optoelectronics," *Chemical Reviews* 124, no. 3 (2024): 768–859, https://doi.org/10.1021/acs.chemrev.3c00548.

14. P. Zhang, Y. Sun, J. Sun, S. Wang, R. Wang, and J. Zhang, "Progress in 2D Material-Based Infrared Photodetectors for Intelligent Vision Applications," *Advanced Functional Materials* 35, no. 36 (2025): 2502072, https://doi.org/10.1002/adfm.202502072.

15. D. Shakthivel, A. Singh Dahiya, and R. Dahiya, "Inorganic Semiconducting Nanostructures-Based Printed Photodetectors," *Applied Physics Reviews* 12, no. 1 (2025): 011325, https://doi.org/10.1063/5.0236154.

16. C. Yang, C. Ji, S. Feng, Y. Liu, W. Wei, and Y. Long, "Ultrafast Laser-Matter Interaction Mechanisms and Applications in Functional Device Fabrication: Recent Advances and Perspectives," *Applied Physics Reviews* 12, no. 3 (2025): 031325, https://doi.org/10.1063/5.0228383.

17. F. Li, T. Shen, C. Wang, Y. Zhang, J. Qi, and H. Zhang, "Recent Advances in Strain-Induced Piezoelectric and Piezoresistive Effect-Engineered 2D Semiconductors for Adaptive Electronics and Optoelectronics," *Nano-Micro Letters* 12, no. 1 (2020): 106, https://doi.org/10.1007/s40820-020-00439-9.

18. Z. Peng, X. Chen, Y. Fan, D. J. Srolovitz, and D. Lei, "Strain Engineering of 2D Semiconductors and Graphene: From Strain Fields to Band-structure Tuning and Photonic Applications," *Light: Science & Applications* 9, no. 1 (2020): 190, https://doi.org/10.1038/s41377-020-00421-5.

19. X. Hou, T. Jin, Y. Zheng, and W. Chen, "Atomic-Scale Interface Engineering for Two-Dimensional Materials based Field-Effect Transistors," *SmartMat* 5, no. 4 (2024): 1236, https://doi.org/10.1002/smm2.1236.

20. J. He, J. Yan, T. Xue, et al., “Terminal Passivation–Induced Interface Decoupling for High-Stability Two-Dimensional Semiconductors,” *SmartMat* 6, no. 2 (2025): 1318, https://doi.org/10.1002/smm2.1318.

21. Y. Chen, N. Cui, X. Li, et al., “A Homogenous Polymer Design With Widely Tunable Work Functions for High-Performance Two-Dimensional Photodetectors,” *Reports on Progress in Physics* 88, no. 6 (2025): 068003, https://doi.org/10.1088/1361-6633/ade006.

22. M. Yang, K. Gong, Y. Cui, S. Liu, G. Li, and S. Lin, “Band Engineering and Structural-Geometrical Engineering in 2D/3D Van Der WAALS Heterostructures for Advanced Photodetection and Intelligent Sensing,” *Nano-Micro Letters* 18, no. 1 (2026): 298, https://doi.org/10.1007/s40820-026-02129-4.

23. J. Wu, B. Shao, Y. Ye, et al., “Broadband and High-resolution Snapshot Spectroscopy With High-index Transition Metal Dichalcogenides,” *Nature Communications* 17, no. 1 (2026): 1955, https://doi.org/10.1038/s41467-026-68685-w.

24. H. Zhao, Z. Tu, and L. Chang, “Recent Advances in Heterogeneous Photonic Integration: From Devices to System-Level Applications,” *PhotoniX Synergy* 1, no. 1 (2026): 5, https://doi.org/10.1007/s44519-026-00013-7.

25. S. Yang, Y. Chen, and C. Jiang, “Strain Engineering of Two-Dimensional Materials: Methods, Properties, and Applications,” *Infomat* 3, no. 4 (2021): 397–420, https://doi.org/10.1002/inf2.12177.

26. R. Ai, X. Cui, Y. Li, and X. Zhuo, “Local Strain Engineering of Two-Dimensional Transition Metal Dichalcogenides towards Quantum Emitters,” *Nano-Micro Letters* 17, no. 1 (2025): 104, https://doi.org/10.1007/s40820-024-01611-1.

27. L. Li, H. Lin, Y. Huang, et al., “High-Performance Flexible Waveguide-Integrated Photodetectors,” *Optica* 5, no. 1 (2018): 44–51, https://doi.org/10.1364/OPTICA.5.000044.

28. M. Rabeel, H. Kim, M. Asghar Khan, et al., “Broadband and Flexible Photodiode of a Bromine-Doped Lateral $MoTe_2$ Homojunction,” *ACS Photonics* 10, no. 12 (2023): 4425–4436, https://doi.org/10.1021/acsphotonics.3c01281.

29. Y. Zou, Z. Zhang, J. Yan, et al., “High-temperature Flexible WSe_2 Photodetectors With Ultrahigh Photoresponsivity,” *Nature Communications* 13, no. 1 (2022): 4372, https://doi.org/10.1038/s41467-022-32062-0.

30. M. F. Khan, S. Sadaqat, M. A. Khan, et al., “Broadening Spectral Responses and Achieving Environmental Stability in SnS_2/Ag-NPs/HfO_2 Flexible Phototransistors,” *Nanoscale* 16, no. 7 (2024): 3622–3630, https://doi.org/10.1039/D3NR04626E.

31. S. Yang, Y. Liu, Y. Wu, et al., “High-performance Flexible Photodetectors Based on CdTe/MoS_2 Heterojunction,” *Nanoscale* 16, no. 29 (2024): 13932–13937, https://doi.org/10.1039/D4NR01718H.

32. T.-L. Shen, Y.-W. Chu, Y.-K. Liao, et al., “Ultrahigh-Performance Self-Powered Flexible Photodetector Driven From Photogating, Piezo-Phototronic, and Ferroelectric Effects,” *Advanced Optical Materials* 8, no. 1 (2020): 1901334, https://doi.org/10.1002/adom.201901334.

33. Q. Li, J. Huang, J. Meng, and Z. Li, “Enhanced Performance of a Self-Powered ZnO Photodetector by Coupling LSPR-Inspired Pyro-Phototronic Effect and Piezo-Phototronic Effect,” *Advanced Optical Materials* 10, no. 7 (2022): 2102468, https://doi.org/10.1002/adom.202102468.

34. S. Pal, A. Ghorai, S. Mahato, and S. K. Ray, “Piezo-Phototronic Effect-Induced Self-Powered Broadband Photodetectors using Environmentally Stable α-$CsPbI_3$ Perovskite Nanocrystals,” *Advanced Optical Materials* 11, no. 16 (2023): 2300233, https://doi.org/10.1002/adom.202300233.

35. Y. Pei, Y. Kang, X. Zhou, et al., “Strain-Modulated Dominant Response Band of Self-Powered Photodetector Based on WSe_2 Lateral PN Homojunction,” *Small* 21, no. 7 (2024): 2410773, https://doi.org/10.1002/smll.202410773.

36. W. Cai, J. Wang, Y. He, et al., “Strain-Modulated Photoelectric Responses From a Flexible α-In_2Se_3/3R MoS_2 Heterojunction,” *Nano-Micro Letters* 13, no. 1 (2021): 74, https://doi.org/10.1007/s40820-020-00584-1.

37. Y. Zhao, F. Guo, R. Ding, et al., “Piezo-Phototronic Effect in 2D α-In_2Se_3/WSe_2 Van Der Waals Heterostructure for Photodetector With Enhanced Photoresponse,” *Advanced Optical Materials* 9, no. 20 (2021): 2100864, https://doi.org/10.1002/adom.202100864.

38. W. Li, M. Dai, Y. Hu, et al., “Synchronous Enhancement for Responsivity and Response Speed in In_2Se_3 Photodetector Modulated by Piezoresistive Effect,” *ACS Applied Materials & Interfaces* 11, no. 50 (2019): 47098–47105, https://doi.org/10.1021/acsami.9b17448.

39. Z. Zhang, L. Li, J. Horng, et al., “Strain-Modulated Bandgap and Piezo-Resistive Effect in Black Phosphorus Field-Effect Transistors,” *Nano Letters* 17, no. 10 (2017): 6097–6103, https://doi.org/10.1021/acs.nanolett.7b02624.

40. C. Lan, Z. Zhou, Z. Zhou, et al., “Wafer-scale Synthesis of Monolayer WS_2 for High-performance Flexible Photodetectors by Enhanced Chemical Vapor Deposition,” *Nano Research* 11, no. 6 (2018): 3371–3384, https://doi.org/10.1007/s12274-017-1941-4.

41. P. Gant, P. Huang, D. Pérez de Lara, D. Guo, R. Frisenda, and A. Castellanos-Gomez, “A Strain Tunable Single-Layer MoS_2 Photodetector,” *Materials Today* 27 (2019): 8–13, https://doi.org/10.1016/j.mattod.2019.04.019.

42. R. Maiti, C. Patil, M. A. S. R. Saadi, et al., “Strain-engineered High-responsivity $MoTe_2$ Photodetector for Silicon Photonic Integrated Circuits,” *Nature Photonics* 14, no. 9 (2020): 578–584, https://doi.org/10.1038/s41566-020-0647-4.

43. Y. Wang, J. Jing, Y. Luo, et al., “Self-Powered, Ultrathin, Flexible, and Scalable Ultraviolet Detector Utilizing a Diamond–MoS_2 Heterojunction,” *Nano Letters* 25, no. 45 (2025): 16115–16122, https://doi.org/10.1021/acs.nanolett.5c04062.

44. S. Aftab, M. Zahir Iqbal, M. W. Iqbal, and M. A. Shehzad, “Strain-Enhanced Photovoltaic Effect in $MoTe_2$,” *Laser & Photonics Reviews* 17 (2023): 2200429.

45. Y. He, Y. Hu, M. Peng, et al., “One-Dimensional Crystal-Structure Te–Se Alloy for Flexible Shortwave Infrared Photodetector and Imaging,” *Nano Letters* 24, no. 19 (2024): 5774–5782, https://doi.org/10.1021/acs.nanolett.4c00881.

46. Y. Xia, J. Zhang, T. Guo, et al., “High-Speed Flexible Near-Infrared Organic Photodetectors for Self-Powered Optical Integrated Sensing and Communications,” *Advanced Functional Materials* 35, no. 2 (2025): 2412813, https://doi.org/10.1002/adfm.202412813.

47. Q. Zhang, S. Ni, D. Zhang, et al., “Multicolor and Polarization-Sensitive Photodetection of α-In_2Se_3/2H-$MoTe_2$ vdW Heterostructure for Imaging and Optical Communication,” *ACS Applied Materials & Interfaces* 17, no. 21 (2025): 31248–31256, https://doi.org/10.1021/acsami.5c04228.

48. J. Wu, Y. Ye, J. Jian, et al., “Reversible Thermally Driven Phase Change of Layered In_2Se_3 for Integrated Photonics,” *Nano Letters* 23, no. 14 (2023): 6440–6448, https://doi.org/10.1021/acs.nanolett.3c01247.

49. J. Wu, J. Jian, H. Ma, et al., “Nonvolatile Electro-optic Response of Graphene Driven by Ferroelectric Polarization,” *Nano Letters* 24, no. 37 (2024): 11469–11475, https://doi.org/10.1021/acs.nanolett.4c02625.

50. J. Wu, J. Jian, B. Sun, et al., “Dual-function Optical Modulation and Detection in Microring Resonators Integrated Graphene/$MoTe_2$ Heterojunction,” *Applied Physics Reviews* 11, no. 2 (2024): 021426, https://doi.org/10.1063/5.0207874.

51. J. Wu, M. Wei, J. Mu, et al., “High-Performance Waveguide-Integrated Bi_2O_2Se Photodetector for Si Photonic Integrated Circuits,” *ACS Nano* 15, no. 10 (2021): 15982–15991, https://doi.org/10.1021/acsnano.1c04359.

52. Y. Jian, X. Song, X. Wang, et al., “ReS_2 /Black Arsenic–Phosphorus van der Waals Heterojunction for a High-Performance Photodetector,” *ACS Applied Electronic Materials* 4, no. 12 (2022): 6013–6019, https://doi.org/10.1021/acsaelm.2c01174.

53. H. Ma, S. Lin, T. He, et al., “Low-Noise Te/$MoTe_2$ Heterojunction Waveguide-Integrated Photodetector,” *ACS Photonics* 11 (2024): 3982–3990.

54. S. Tian, M. Jia, T. Xu, et al., “Strain-enhanced Image Recognition via Piezo-phototronic Effect in MnSe/α-In_2Se_3 Heterostructure Photodetector,” *Nano Research* 19, no. 4 (2026): 94908320, https://doi.org/10.26599/NR.2026.94908320.

55. C. Ruppert, B. Aslan, and T. F. Heinz, “Optical Properties and Band Gap of Single- and Few-Layer $MoTe_2$ Crystals,” *Nano Letters* 14, no. 11 (2014): 6231–6236, https://doi.org/10.1021/nl502557g.

56. S. Bok Seo, S. Nah, M. Sajjad, S. Ho Suk, and S. Sim, “Slow Hot Carrier Cooling and Quasi-Fermi Shift Dynamics in Few-Layer α-In_2Se_3 via Transient Absorption Spectroscopy,” *Advanced Optical Materials* 13 (2025): 2403531.

57. J. Ahn, J.-H. Kyhm, H. K. Kang, N. Kwon, H.-K. Kim, and S. Park, “2D $MoTe_2$ /ReS_2 van der Waals Heterostructure for High-Performance and Linear Polarization-Sensitive Photodetector,” *ACS Photonics* 8, no. 9 (2021): 2650–2658, https://doi.org/10.1021/acsphotonics.1c00598.

58. J. Wang, C. Liu, L. Zhang, et al., “Selective Enhancement of Photoresponse With Ferroelectric-Controlled BP/In_2Se_2 vdW Heterojunction,” *Advanced Science* 10, no. 11 (2023): 2205813, https://doi.org/10.1002/advs.202205813.

59. W. Wu, L. Wang, Y. Li, et al., “Piezoelectricity of Single-atomic-layer MoS_2 for Energy Conversion and Piezotronics,” *Nature* 514, no. 7523 (2014): 470–474, https://doi.org/10.1038/nature13792.

60. W. Wu and Z. L. Wang, “Piezotronics and Piezo-phototronics for Adaptive Electronics and Optoelectronics,” *Nature Reviews Materials* 1, no. 7 (2016): 16031, https://doi.org/10.1038/natrevmats.2016.31.

61. W. Wu, L. Wang, R. Yu, et al., “Piezophototronic Effect in Single-Atomic-Layer MoS_2 for Strain-Gated Flexible Optoelectronics,” *Advanced Materials* 28, no. 38 (2016): 8463–8468, https://doi.org/10.1002/adma.201602854.

Supporting Information

Additional supporting information can be found online in the Supporting Information section.

Supporting File: adom71739-sup-0001-SuppMat.docx.